INTERNATIONAL JOURNAL FOR NUMERICAL METHODS IN FLUIDS
Int. J. Numer. Meth. Fluids 2008; **57**:977–1003
Published online 17 December 2007 in Wiley InterScience (www.interscience.wiley.com). DOI: 10.1002/fld.1660

A numerical strategy for the direct 3D simulation of the expansion of bubbles into a molten polymer during a foaming process

J. Bruchon*,† and T. Coupez

CEMEF, UMR CNRS 7635, Ecole des Mines de Paris, Rue Claude Daunesse, BP 207, 06904 Sophia Antipolis, Cedex, France

SUMMARY

In the framework of the foam process modelling, this paper presents a numerical strategy for the direct 3D simulation of the expansion of gas bubbles into a molten polymer. This expansion is due to a gas overpressure. The polymer is assumed to be incompressible and to behave as a pseudo-plastic fluid. Each bubble is governed by a simple ideal gas law. The velocity and the pressure fields, defined in the liquid by a Stokes system, are subsequently extended to each bubble in a way of not perturbing the interface velocity. Hence, a global velocity–pressure-mixed system is solved over the whole computational domain, thanks to a discretization based on an unstructured first-order finite element. Since dealing with an Eulerian approach, an interface capturing method is used to follow the bubble evolution. For each bubble, a pure advection equation is solved by using a space–time discontinuous-Galerkin method, coupled with an r-adaptation technique. Finally, the numerical strategy is achieved by considering a global mesh expansion motion, which conserves the amount of liquid into the computational domain during the expansion. The expansion of one bubble is firstly considered, and the simulations are compared with an analytical model. The formation of a cellular structure is then investigated by considering the expansion of 64 bubbles in 2D and the expansion of 400 bubbles in 3D. Copyright © 2007 John Wiley & Sons, Ltd.

Received 29 November 2006; Revised 1 June 2007; Accepted 4 October 2007

KEY WORDS: liquid–gas interaction; VOF method; mesh r-adaptation technique; change of scale; bubble expansion; cellular structure

1. INTRODUCTION

A polymer foam can be produced by a wide variety of processes, ranging from expandable beads to injection molding and extrusion. However, these processes include, on a macroscopic scale,

*Correspondence to: J. Bruchon, CEMEF, UMR CNRS 7635, Ecole des Mines de Paris, Rue Claude Daunesse, BP 207, 06904 Sophia Antipolis, Cedex, France.
†E-mail: julien.bruchon@ensmp.fr

Contract/grant sponsor: EU BIOFOAM Programme, Quality of Life and Management of Living Resources; contract/grant number: QLRT-1999-01298

two common stages: the nucleation of a dense population of gas clusters in a supersaturated solution and the subsequent growth of the nucleated bubbles. These two steps largely determine the characteristics of the foam cellular structure, and are the purpose of a lot of papers in the literature [1–4].

This work is concerned only with the simulation of the expansion step during an injection or an extrusion process. In this case, the expansion is a consequence of the sudden drop of pressure, which occurs when the bubbly melt is injected into the mold (in an injection process) or when it flows out of the die (in an extrusion process). Our aim is to simulate and to characterize, on a mesoscopic scale, the formation of a foam cellular structure during such processes. In other words, a foam sample is assumed to be a set of bubbles embedded into a polymeric matrix, with an initial gas overpressure. The aim is then to simulate the bubble expansion and the bubble interaction, until a cellular structure is obtained. In the literature, this kind of mesoscopic approach is generally based on the cell model, which has been introduced by Amon and Denson in [5] (see, for example, [6–10]). This model provides the evolution of the radius of a spherical bubble growing into a finite volume of polymer. This evolution is related to the difference between the bubble inner pressure (which is a parameter calculated by the cell model) and the liquid ambient pressure (which is a macroscopic parameter, seen as an input data of the model). A micro–macro coupling can then be considered [11] through the foam density. This density depends on the local bubble radius, and therefore on the local pressure.

The cell model reduces the simulation of foam structure formation to the resolution of an ordinary differential equation governing the radius evolution. However, a foam structure is much more complex than a stack of spherical cells. Indeed, during their expansion, the bubbles interact with each other, recovering a wide variety of shapes [4]. Such morphological changes cannot be described by the cell model. In that sense, the cell model is not completely relevant to investigate the formation of a foam structure on a mesoscopic scale.

Contrary to the usual cell model, this work assumes neither any particular bubble shape nor a fixed number of bubbles. The expansion of the bubbles into a liquid matrix is directly simulated by using a finite element approach. The strategy used to perform such simulations is developed in Section 2. The mechanical equations, the liquid–gas coupling and the resulting weak formulation are first exposed. An interface capturing technique, based on a space–time discontinuous-Galerkin method, coupled with a mesh r-adaptation method is then briefly described. The change of scale induced by the bubble expansion is taken into account through a global expansion motion. Section 3 deals with the expansion of one bubble. Different cases are distinguished: constant gas pressure, ideal gas law, Newtonian matrix and non-Newtonian matrix. Finally, simulations involving a large number of bubbles are investigated in Section 4 for the two-dimensional case and in Section 5 for the three-dimensional case. Here, a special treatment is required to reduce the memory cost and the central processing unit (CPU) time of the simulations.

2. MATHEMATICAL FORMULATION

Let us consider the computational domain Ω, a bounded region of $\mathbb{R}^d$ (a square if $d=2$, a cube if $d=3$), filled with a gas domain Ω_{g} embedded into a polymeric liquid matrix Ω_l (see Figure 1). The domain Ω is defined as a representative elementary volume (REV) of an expanding foam. Polymer and gas are assumed to be immiscible. The gas domain is considered as a set of n distinct bubbles Ω_{g_i} : $\Omega_{\mathrm{g}}=\bigcup_{i=1}^{n}\Omega_{\mathrm{g}_i}$. At a polymer–bubble interface, the gas exerts a stress $-p_{\mathrm{g}_i}\mathbf{n}$ on the

DOI: 10.1002/fld

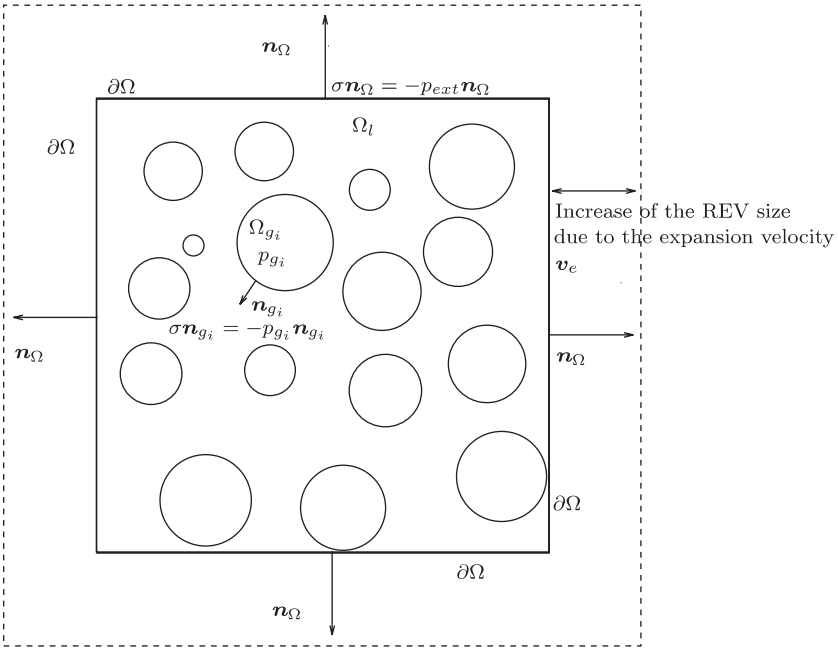

Figure 1. Expansion of a set of bubbles Ω_{g_i} into a liquid matrix Ω_l (REV).

polymer, where p_{g_i} is the bubble inner pressure. Under this stress, the polymer flows through the boundary of Ω, allowing the bubble to expand: the increase of the bubble volume gives rise to the decrease of the bubble pressure, according to the ideal gas law. A bubble reaches its equilibrium state when $p_{g_i} = p_{ext}$, where p_{ext} is the macroscopic stress imposed over $\partial\Omega$. Hence, the gas expansion is only due to the difference between the gas pressure and the ambient pressure. The gas diffusion is not taken into account in our simulations. Furthermore, as implicitly mentioned in the above equilibrium condition, the surface tension effects are neglected. The relevance of this assumption can be investigated by evaluating the capillary number $Ca = \eta_l U/\gamma$, where η_l is the polymer viscosity in the range of 10^3 (Pa s), γ is the surface tension coefficient in the range of 10^{-2} (N/m), and U is a characteristic velocity [3]. Literature results [5, 12] show that during the foam expansion step, we have $Ca \gg 1$, and then the surface tension effects can be neglected. In another context, these effects have been investigated by [13], using an approach similar to the approach presented here, but for small 2D bubble clusters.

The numerical methodology developed in this paper is based on an Eulerian approach: the bubbles evolve through a 'fixed' mesh on the whole computational domain. An additional function (a characteristic function) is then used for capturing the liquid–gas interfaces. Such a strategy is convenient to treat the large deformations of the liquid–gas interfaces, which are involved in the expansion. Since the whole computational domain Ω is meshed, the velocity and the pressure fields $\mathbf{v}$ and p must be defined over all Ω. Equations governing these fields are first established in the liquid matrix, and subsequently extended to the gas domain. Furthermore, since the interfaces are not explicitly defined, the interface conditions have to be turned in terms of equivalent volume conditions.

DOI: 10.1002/fld

2.1. Conservation equations in the liquid domain

The polymeric matrix is assumed to behave as an incompressible Newtonian fluid. The liquid's Cauchy stress tensor is $\sigma_l = 2\eta_l \varepsilon(\mathbf{v}) - pI$, where $\varepsilon(\mathbf{v})$ is the strain-rate tensor. Note that the viscosity of the liquid, η_l, can be related to the norm of $\varepsilon(\mathbf{v})$ through a power law or Carreau's law, which expresses the shear-thinning behavior of the polymer. However, all the simulations presented in this paper have been carried out by using a constant liquid viscosity, except for the one in Section 3.3.

The influence of inertia can be evaluated through the Reynolds number Re, which is obtained by balancing the inertia term with the viscosity term in the momentum equation. Re is defined in [14] by

$$Re = \frac{\rho V_0^{2/3}(p_g^0 - p_{\text{ext}})}{\eta_l^2} \tag{1}$$

where ρ is the matrix density, V_0 the initial bubble volume and p_g^0 the initial gas pressure. For a molten polymer, we have $\rho/\eta_l^2 \simeq 10^{-3}$. Consequently, since the initial bubble radius is of order 10^{-3} m and the initial pressure difference is of order 10^2 Pa, we have $Re \ll 1$, and the inertia effects are neglected in the following.

Assuming that Ω_l is known, the momentum and mass conservation laws give the Stokes equations governing $\mathbf{v}$ and p:

$$\begin{aligned} \nabla \cdot [2\eta_l \varepsilon(\mathbf{v})] - \nabla p &= 0 \\ \nabla \cdot \mathbf{v} &= 0 \\ \sigma_l \mathbf{n}_{g_i} &= \sigma_{g_i} \mathbf{n}_{g_i} \quad \text{on } \partial\Omega_{g_i} \ \ \forall i = 1, \ldots, n \\ \sigma \mathbf{n}_\Omega &= -p_{\text{ext}} \mathbf{n}_\Omega \quad \text{on } \partial\Omega \end{aligned} \tag{2}$$

In System (2), $\mathbf{n}_{g_i}$ is the unit normal pointing outward Ω_{g_i}, and $\mathbf{n}_\Omega$ is the unit normal pointing outward Ω_l (and pointing therefore outward Ω). The macroscopic stress imposed over $\partial\Omega$ (we assume that $\partial\Omega \cap \Omega_{g_i} = \emptyset$) is denoted by $-p_{\text{ext}}\mathbf{n}_\Omega$. The macroscopic parameter p_{ext} represents the ambient pressure in the liquid matrix (see Section 3.1). Finally, σ_{g_i} is the Cauchy stress tensor of the ith bubble.

2.2. Conservation equations in a gas bubble

A gas bubble Ω_{g_i} is only governed by the ideal gas law, which relates the inner pressure p_{g_i} to the bubble volume $|\Omega_{g_i}|$. In the isothermal case, this relation is

$$p_{g_i} |\Omega_{g_i}| = C_i \tag{3}$$

In expression (3), each C_i is a constant. The drawback of such a quasi-static description is that only the average pressure is known inside each bubble (this pressure is uniform), while it does not allow describing the velocity inside the gas domain. This means that the bubble growth is described by the velocity of the liquid at the interface, which moves by the pressure difference.

DOI: 10.1002/fld

Consequently, the velocity field, already defined in Ω_l, is extended to Ω_{g_i} in such a way so as to not perturb the interfacial velocity:

$$\begin{gathered}\mathbf{v} \in \mathscr{C}^1(\Omega) \\ 2\eta_g \nabla \cdot [\varepsilon(\mathbf{v})] = 0 \quad \text{in } \Omega_{g_i}\end{gathered} \tag{4}$$

where η_g is a (small) numerical parameter, called gas viscosity. This extension (4) is equivalent to add a viscosity term to the bubble Cauchy stress tensor $\sigma_{g_i} = 2\eta_g \varepsilon(\mathbf{v}) - p_{g_i} I$. The numerical parameter η_g has to be chosen small enough so that

$$2\eta_g \|\varepsilon(\mathbf{v})\mathbf{n}_{g_i}\|_{\mathbb{R}^d} \ll \|p_{g_i}\mathbf{n}_{g_i}\|_{\mathbb{R}^d} = p_{g_i} \quad \text{on } \partial\Omega_{g_i} \tag{5}$$

Under this condition, the consistency of this approach is ensured in the sense that

$$\sigma_{g_i} \approx -p_{g_i} I \quad \text{in } \Omega_{g_i}$$

Finally, the pressure field p, already defined in Ω_l, has to be extended in Ω_{g_i}. A natural extension is to set a uniform pressure inside each bubble:

$$p = p_{g_i} \quad \text{in } \Omega_{g_i} \tag{6}$$

However, note that since σ_{g_i} is directly related to the bubble pressure p_{g_i} and not to the pressure field p, the value of p in the gas domain is never used in Equations (2). Consequently, extension (6) is only a numerical device to have a pressure field p defined on the whole computational domain, leading to an inversible finite element system (see [13]).

2.3. Velocity–pressure-mixed variational formulation

The following functional spaces are first introduced: $\mathscr{V} = (H^1(\Omega))^d$ and $\mathscr{P} = L^2(\Omega)$. The global mixed formulation is obtained by adding the weak forms of System (2) to those of Equations (4) and (6). More precisely, considering that $\mathbf{n}_\Omega = -\mathbf{n}_{g_i}$, the variational formulation of System (2) in the liquid matrix is straightforward:

$$\begin{gathered}\int_{\Omega_l} 2\eta_l \varepsilon(\mathbf{v}) : \varepsilon(\mathbf{w})\,\mathrm{d}\Omega - \int_{\Omega_l} p\nabla\cdot\mathbf{w}\,\mathrm{d}\Omega = -\int_{\partial\Omega} p_{\text{ext}}\mathbf{w}\cdot\mathbf{n}_\Omega\,\mathrm{d}\Gamma - \sum_{i=1}^{n}\int_{\partial\Omega_{g_i}} \sigma_{g_i}\mathbf{n}_{g_i}\cdot\mathbf{w}\,\mathrm{d}\Gamma \\ \int_{\Omega_l} q\nabla\cdot\mathbf{v}\,\mathrm{d}\Omega = 0 \quad \forall(\mathbf{w}, q) \in \mathscr{V}\times\mathscr{P}\end{gathered} \tag{7}$$

The weak formulation in the gas domain is obtained in a similar way:

$$\begin{gathered}\int_{\Omega_g} 2\eta_g \varepsilon(\mathbf{v}) : \varepsilon(\mathbf{w})\,\mathrm{d}\Omega = \sum_{i=1}^{n}\int_{\partial\Omega_{g_i}} (\sigma_{g_i}\mathbf{n}_{g_i} + p_{g_i}\mathbf{n}_{g_i})\cdot\mathbf{w}\,\mathrm{d}\Gamma \\ \int_{\Omega_g} pq\,\mathrm{d}\Omega = \sum_{i=1}^{n} p_{g_i}\int_{\Omega_{g_i}} q\,\mathrm{d}\Omega \quad \forall(\mathbf{w}, q) \in \mathscr{V}\times\mathscr{P}\end{gathered} \tag{8}$$

Finally, the global mixed formulation results from the addition of Systems (7) and (8) and from the use of the divergence theorem to turn the surface integral involving the pressure of the bubbles into volume integral.

DOI: 10.1002/fld

Find $(\mathbf{v}, p) \in \mathscr{V} \times \mathscr{P}$ such that

$$\begin{aligned}
&\int_{\Omega_l} 2\eta_l \varepsilon(\mathbf{v}) : \varepsilon(\mathbf{w})\, \mathrm{d}\Omega + \int_{\Omega_\mathrm{g}} 2\eta_\mathrm{g} \varepsilon(\mathbf{v}) : \varepsilon(\mathbf{w})\, \mathrm{d}\Omega - \int_{\Omega_l} p \nabla \cdot \mathbf{w}\, \mathrm{d}\Omega \\
&\quad = -\int_{\partial\Omega} p_\mathrm{ext} \mathbf{w} \cdot \mathbf{n}_\Omega\, \mathrm{d}\Gamma + \sum_{i=1}^{n} p_{\mathrm{g}_i} \int_{\Omega_{\mathrm{g}_i}} \nabla \cdot \mathbf{w}\, \mathrm{d}\Omega \\
&\qquad - \int_{\Omega_l} q \nabla \cdot \mathbf{v}\, \mathrm{d}\Omega - \alpha_p \int_{\Omega_\mathrm{g}} pq\, \mathrm{d}\Omega = -\alpha_p \sum_{i=1}^{n} p_{\mathrm{g}_i} \int_{\Omega_{\mathrm{g}_i}} q\, \mathrm{d}\Omega \quad \forall (w, q) \in \mathscr{V} \times \mathscr{P}
\end{aligned} \tag{9}$$

The second equation of (8) is necessary to guarantee that the final System (9) is inversible. This System (9) is closed with the n scalar equations (3). The numerical parameter α_p has the dimensions of the inverse of viscosity. It has to be chosen small enough to ensure the mass conservation in the liquid domain in the discrete case. In practice, we take $\alpha_p = 10^{-5}$ in all the simulations presented in this paper.

A solution of Systems (2), (4) and (6) is also solution of the weak formulation (9). Consequently, the solution $(\mathbf{v}, p)$ of (9) satisfies implicitly the following relation, which expresses the continuity of the normal stress across $\partial\Omega_{\mathrm{g}_i}$:

$$\int_{\partial\Omega_{\mathrm{g}_i}} \sigma \mathbf{n}_{\mathrm{g}_i} \cdot w\, \mathrm{d}\Gamma = \int_{\partial\Omega_{\mathrm{g}_i}} ((2\eta_\mathrm{g} \varepsilon(\mathbf{v}) - p_{\mathrm{g}_i} I)\mathbf{n}_{\mathrm{g}_i}) \cdot w\, \mathrm{d}\Gamma \tag{10}$$

Hence, the weak formulation (9) is consistent with the initial problem.

Finally, in order to solve Equations (9) by using a finite element method, the integrals defined over Ω_l and Ω_{g_i} have to be turned into integrals defined over the whole computational domain Ω. This operation is performed by introducing the n characteristic functions of the bubbles, $\mathbb{1}_{\Omega_{\mathrm{g}_i}}$ ($\mathbb{1}_{\Omega_{\mathrm{g}_i}}$ is equal to 1 in Ω_{g_i} and is vanishing elsewhere), the characteristic function of the gas domain $\mathbb{1}_{\Omega_\mathrm{g}}$ ($\mathbb{1}_{\Omega_\mathrm{g}} = \sum_{i=1}^{n} \mathbb{1}_{\Omega_{\mathrm{g}_i}}$) and the characteristic function of the liquid matrix, $\mathbb{1}_{\Omega_l}$ ($\mathbb{1}_{\Omega_l} = 1 - \mathbb{1}_{\Omega_\mathrm{g}}$). Multiplying the integrand by $\mathbb{1}_{\Omega_l}$ (or $\mathbb{1}_{\Omega_{\mathrm{g}_i}}$) will restrict the integral to Ω_l (or Ω_{g_i}):

$$\int_{\Omega_l} f\, \mathrm{d}\Omega = \int_{\Omega} \mathbb{1}_{\Omega_l} f\, \mathrm{d}\Omega, \quad \int_{\Omega_{\mathrm{g}_i}} f\, \mathrm{d}\Omega = \int_{\Omega} \mathbb{1}_{\Omega_{\mathrm{g}_i}} f\, \mathrm{d}\Omega, \quad \int_{\Omega_\mathrm{g}} f\, \mathrm{d}\Omega = \int_{\Omega} \mathbb{1}_{\Omega_\mathrm{g}} f\, \mathrm{d}\Omega \tag{11}$$

The MINI-element is used to discretize the resulting mixed formulation. This finite element, introduced in [15], is a first-order element with a linear continuous interpolation of both pressure and velocity, and a bubble enrichment of the velocity. This bubble function, which is necessary to satisfy the LBB stability condition (cf. [16]), can be seen as an enrichment of the element by four piecewise linear functions.

Finally, the finite element implementation is achieved by computing the characteristic functions of the bubbles $\mathbb{1}_{\Omega_{\mathrm{g}_i}}$, i.e. by computing the evolution of the bubbles over time.

DOI: 10.1002/fld

2.4. *Interface capturing method*

Each characteristic function $\mathbb{1}_{\Omega_{g_i}}$ satisfies the following pure advection equation:

$$\begin{cases} \dfrac{\partial \mathbb{1}_{\Omega_{g_i}}}{\partial t} + \mathbf{v}_c \cdot \nabla \mathbb{1}_{\Omega_{g_i}} = 0 & \text{in } \Omega \\ \mathbb{1}_{\Omega_{g_i}}(x,0) = \mathbb{1}_{\Omega_{g_i}0}(x) & \text{in } \Omega \\ \mathbb{1}_{\Omega_{g_i}}(x,t) = g(x,t) & \text{on } \partial\Omega^- \end{cases} \tag{12}$$

The boundary condition g is imposed at the inflow of $\partial\Omega$, $\partial\Omega^- = \{x \in \partial\Omega;\ \mathbf{v}_c(x) \cdot \mathbf{n}(x) < 0\}$. The convective velocity $\mathbf{v}_c$ is defined as $\mathbf{v}_c = \mathbf{v} - \mathbf{v}_{mesh}$. The mesh velocity $\mathbf{v}_{mesh}$ results from the addition of a mesh r-adaptation velocity with a global mesh expansion velocity: $\mathbf{v}_{mesh} = \mathbf{v}_{adapt} + \mathbf{v}_e$ (see next sections).

Solving such a pure advection equation (12) is still a difficult numerical challenge. Indeed, it may lead to spurious oscillations when using standard finite element methods [17] or to an important diffusion of the interfaces. The problem is that since the characteristic functions are discontinuous at the liquid–gas interfaces, they have steep gradients in these zones.

A space–time discontinuous-Galerkin method has been developed to solve equations such as (12). This method, which belongs to the set of volume of fluid (VOF) method, is implicit in time and does not require any Courant–Friedrichs–Lewy (CFL) condition. The discontinuities of the characteristic function are taken into account in a natural way by using a discontinuous approximation in space and time, constant on each space element (tetrahedron) and polynomial of degree q on each time interval. Further details are given in [18].

The value on a spatial element K of the approximated function $\mathbb{1}^h_{\Omega_{g_i}}$ is equal to the local volume fraction of $\Omega^h_{g_i}$: $\mathbb{1}^h_{\Omega_{g_i}|K} = |\Omega^h_{g_i} \cap K|/|K|$ (see [19]). Hence, contrary to the exact solution $\mathbb{1}_{\Omega_{g_i}}$, $\mathbb{1}^h_{\Omega_{g_i}}$ does not only take two values, zero and one, but can also take any value between zero and one. Because of this numerical diffusion phenomenon, the boundary of $\Omega^h_{g_i}$ is not explicitly defined as a discontinuous interface: it contains a region of transition. The level set 0.5 of $\mathbb{1}^h_{\Omega_{g_i}}$ is then chosen to visualize the surface of $\Omega^h_{g_i}$ in our results.

The size of the diffusion zone must be reduced as much as possible to obtain an accurate description of the liquid–gas system evolution. That can be performed by decreasing the time approximation error and by decreasing the space approximation error. 1D and 2D tests show (see [20]) that the time approximation error is largely improved when a $P1$ time approximation is used instead of a $P0$ one. However, taking a higher order ($q > 1$) does not seem to be relevant: the subsequent additional time and memory costs are too important when compared with the solution improvement. It explains that all the simulations presented in this paper have been performed by considering a time approximation order equal to 1 ($q = 1$).

2.4.1. A mesh r-adaptation technique. The diffusion due to the space approximation is reduced by using the mesh r-adaptation technique introduced by Bigot and Coupez in [21]. In this reference, authors have used the following estimator of the local space approximation error: $\mathscr{E}^2_{loc} = \mathbb{1}^h_{\Omega_{g_i}|K}(1 - \mathbb{1}^h_{\Omega_{g_i}|K})|K|$. This estimator corresponds to a $P0$ time approximation ($q = 0$), but can easily be extended to a higher approximation order, as shown in [20]. However, whatever the approximation

DOI: 10.1002/fld

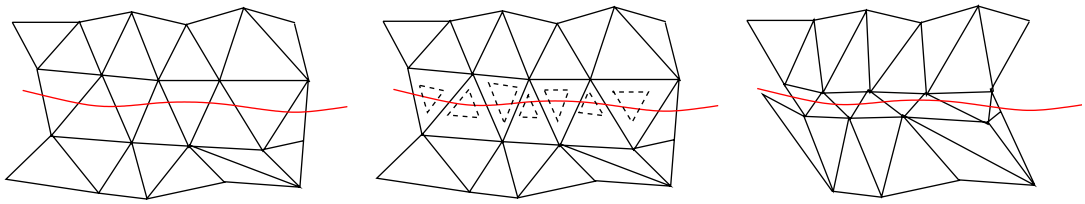

Figure 2. Illustration of the r-adaptation method: initial mesh, target volumes and final mesh.

order q, the key point is that $\mathscr{E}_{\text{loc}}$ can be reduced by decreasing the volume of the interface elements (i.e. elements K such that $0<\mathbb{1}^h_{\Omega_{g_i}|K}<1$). This reduction is performed through a mesh r-adaptation technique, as described in [21]. This technique preserves the mesh topology (no remeshing): only the nodes are moved. For each element, this motion corresponds to a homothety computed to reach a prescribed target volume (see Figure 2).

Contrary to the Lagrangian or Arbitrary Lagrangian Eulerian techniques, the mesh is not distorted as the flow moves, but is stretched in the vicinity of the liquid–gas interfaces, and goes back to a regular shape once these interfaces have passed through. This mesh adaptation motion provides a mesh adaptation velocity field $\mathbf{v}_{\text{adapt}}$, which is the first contribution to the mesh velocity $\mathbf{v}_{\text{mesh}}$.

Finally, note that this space–time approach makes it necessary to integrate over the time interval $[t, t+\Delta t]$ the mixed formulation (9). Here, the velocity and the pressure fields are chosen constant over each time interval.

2.5. *Evolution of the computational scale*

The previous described developments are used to simulate the expansion of a REV containing 125 bubbles. Such an expansion is presented at different steps in Figure 3. More precisely, this figure shows the evolution of the level set 0.5 of the gas volume fraction. Spherical bubbles are initially disposed along a rectangular grid of dimensions $5\times5\times5$. Owing to the pressure difference, the bubbles grow, interact and begin to adopt polyhedral shapes. At the end of the simulation, the liquid remaining in the computational domain is mainly trapped between the bubbles. This gives rise to the cellular structure (cross structure) formation shown in Figure 3(e) and (f). However, beyond a certain level of expansion, the isovalue 0.5 of the gas volume fraction disappears when two bubbles are too close, giving rise to the formation of 'holes' into the structure. This apparent coalescence phenomenon is due to the numerical diffusion, which is reduced but not removed by the mesh r-adaptation. For instance, let us consider two bubble characteristic functions being equal to 0.5 and 0.4, respectively, on a same element. This situation appears in bold in Figure 4. The gas volume fraction is therefore equal to 0.9 on this element, while the liquid function is equal to 0.1. Hence, the value 0.5 does not exist any more! This phenomenon occurs when the gas volume fraction reaches the value of 65–70%, with the meshes used in the presented simulations. Before continuing, it is important to understand that our simulations do not use any coalescence model. The Stokes equations alone cannot provide a criterion to decide if two bubbles are merging. Such a criterion should not only take into account the pressure drop, of course, but also the polymer rheology, the surface tension and some surface active agents, which play an important role in stabilizing the real foams. However, these considerations are beyond the scope of this paper. Here,

DOI: 10.1002/fld

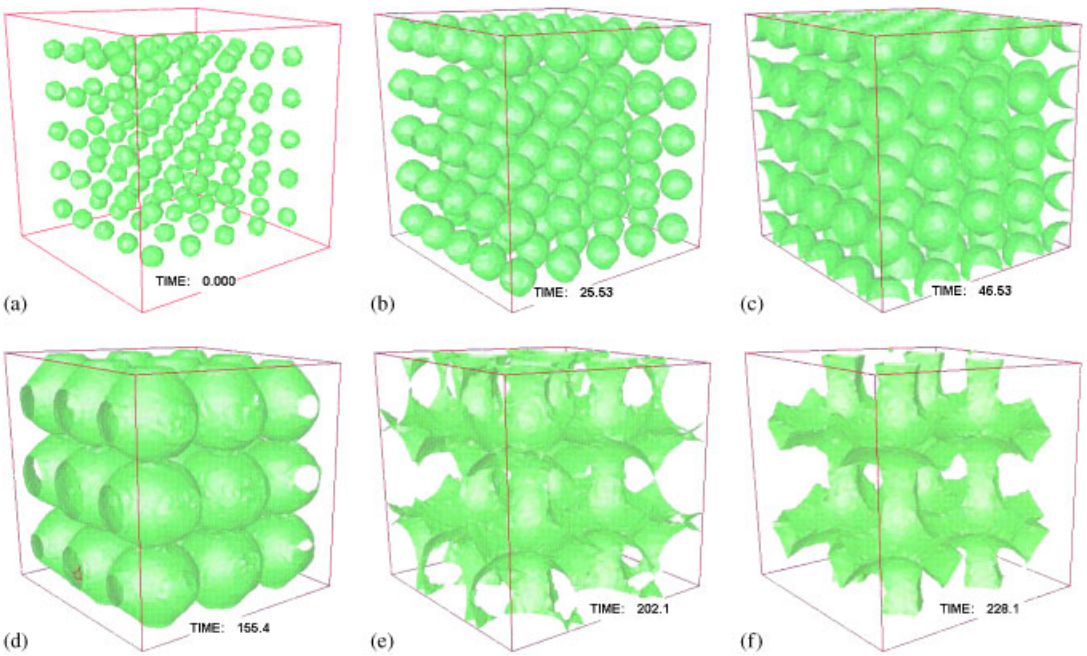

Figure 3. Expansion of 125 bubbles: visualization of the scale change.

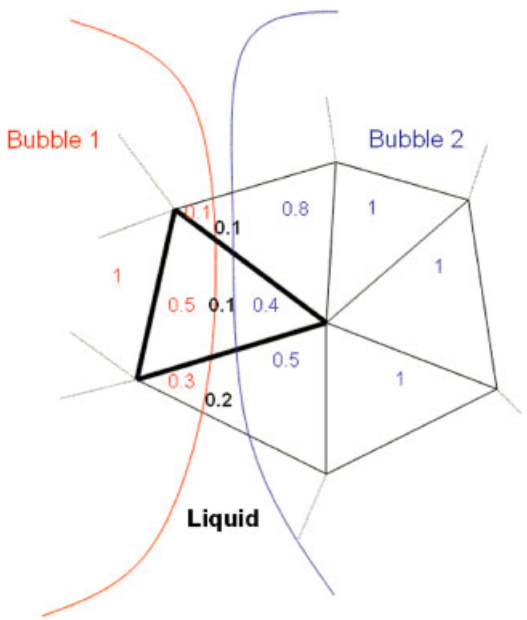

Figure 4. Illustration of the apparent coalescence phenomenon of two bubbles.

DOI: 10.1002/fld

the coalescence is only due to the numerical diffusion of the interfaces and to the local size of the mesh elements.

Let us consider our expansion of 125 bubbles. The key point of this simulation is that, because of the gas expansion, only a few bubbles are still remaining in the REV at the end of the computation. In order to overcome this change of scale, we introduce a global expansion of the REV. This motion is expressed through a mesh expansion velocity $\mathbf{v}_e$, which must verify two conditions: $\mathbf{v}_e$ preserves the computational domain geometry (angles and length ratio), and $\mathbf{v}_e$ preserves the volume of liquid into the computational domain during a simulation. These two conditions lead to the following properties. First, $\mathbf{v}_e$ is a homothety:

$$\mathbf{v}_e(X) = L(X - C) \tag{13}$$

where L is the dilation factor, C is the center of the computational domain while X denotes the coordinates of a mesh node. The second condition is expressed as a flux equality:

$$\int_{\partial\Omega} \mathbf{v}_e \cdot \mathbf{n}\, d\Gamma = \int_{\partial\Omega} \mathbf{v} \cdot \mathbf{n}\, d\Gamma \tag{14}$$

It has to be pointed out that Equation (14) remains relevant while $\partial\Omega \cap \partial\Omega_l = \partial\Omega$. Furthermore, the divergence theorem gives

$$\int_{\Omega} \nabla \cdot \mathbf{v}_e\, d\Omega = \int_{\Omega} \nabla \cdot \mathbf{v}\, d\Omega \tag{15}$$

Combining Equations (13) and (15), we obtain

$$L = \frac{1}{d|\Omega|} \int_{\Omega} \nabla \cdot \mathbf{v}\, d\Omega \tag{16}$$

where d denotes the spatial dimension and $|\Omega|$ the volume of Ω. Finally, taking into account the liquid incompressibility, the equation of the global expansion velocity is

$$\begin{aligned} \frac{dX}{dt} = \mathbf{v}_e(X) &= \frac{X - C}{d|\Omega|} \int_{\Omega_g} \nabla \cdot \mathbf{v}\, d\Omega \\ X(0) &= X^0 \end{aligned} \tag{17}$$

This mesh expansion velocity is the second contribution to the global mesh velocity: $\mathbf{v}_{mesh} = \mathbf{v}_{adapt} + \mathbf{v}_e$. Figure 5 shows results obtained with this technique when considering the previous case (125 bubbles). The amount of liquid and the number of bubbles are then preserved during the expansion, until reaching a gas fraction of about 65%, as shown in Figure 6. Beyond this value, bubbles are too close to the domain boundary, and, due to the numerical diffusion, the flux equality (14) is not relevant any more ($\partial\Omega \cap \partial\Omega_l \neq \partial\Omega$). For the sake of completeness, we have to mention that the matrix volume is not exactly constant when $\partial\Omega \cap \partial\Omega_l = \partial\Omega$ ($t < 100$ in Figure 6), but is slightly increasing. This increase in volume is due to the fact that the liquid incompressibility condition ($\nabla \cdot \mathbf{v} = 0$) is not exactly satisfied in the zone of diffusion of the characteristic functions. Indeed, if we take α_p equal to 10^{-3} instead of 10^{-5} in the second equation of (9) (the equation that ensures the incompressibility), the increase in volume is much more important (see [20]).

DOI: 10.1002/fld

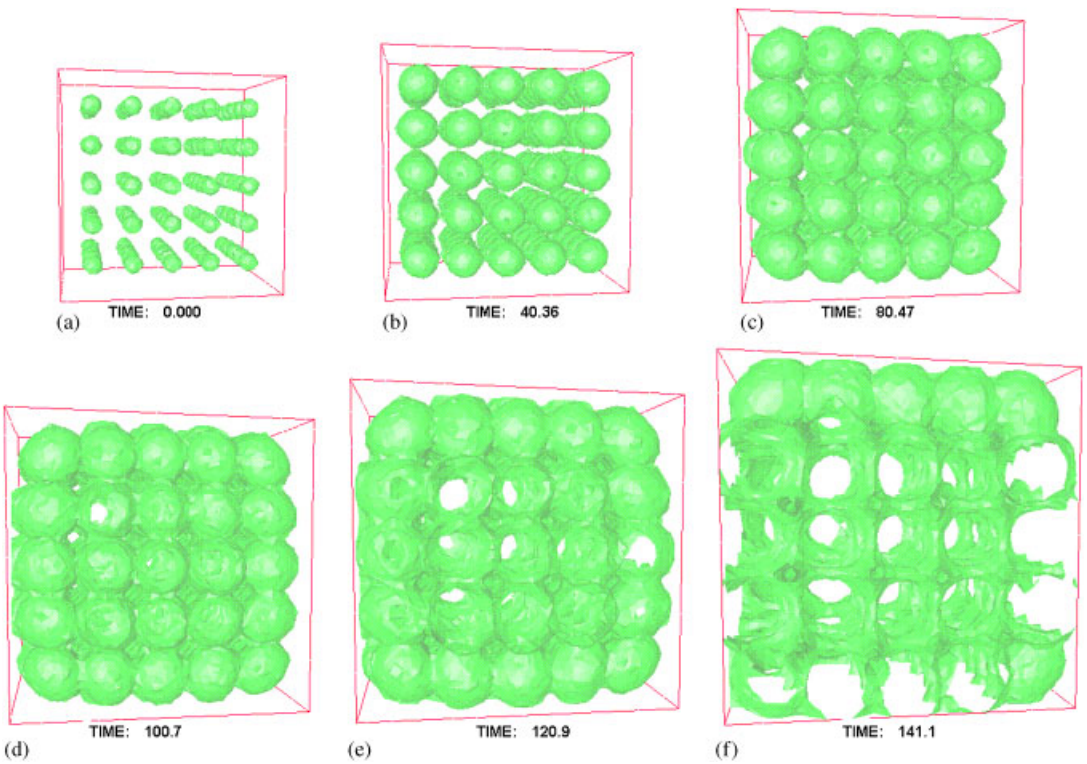

Figure 5. Expansion of 125 bubbles: expansion of the computational domain. G is the gas fraction, V the ratio between the actual computational domain volume and the initial one, while V_f is the volume of the polymer matrix: (a) $G=6\%, V=1, V_f=0.94$; (b) $G=27\%, V=1.28, V_f=0.934$; (c) $G=48\%, V=1.81, V_f=0.941$; (d) $G=57\%, V=2.2, V_f=0.946$; (e) $G=67\%, V=2.66, V_f=0.88$; and (f) $G=79\%, V=3.31, V_f=0.691$.

2.6. Time stepping strategy

To summarize the numerical strategy described, a simulation of the expansion of Nbb bubbles into a liquid matrix will involve the following steps:

- Initialization of the Nbb characteristic functions of the bubbles (for instance, with a random choice of the initial radii and bubble centers, but with a great care that drops are nonoverlapping). These functions are constant over the time interval $I_0=[t_0, t_1]$.
- While the gas volume fraction is lower than a prescribed fraction, do:

For each time interval $I_n=[t_n, t_{n+1}]$, the problem is solved by decoupling the original problem in the following subproblems:

1. Computation of the bubble pressures by solving Equation (3) with $|\Omega_{g_i}|=(1/|I_n|)\times \int_{I_n\times\Omega} \mathbb{1}_{\Omega_{g_i}}\,\mathrm{d}\Omega\,\mathrm{d}t$.
2. Computation of $\mathbf{v}$ and p on I_n by solving the quasi-static Stokes system (9) integrated over I_n.
3. Computation of the mesh r-adaptation velocity $\mathbf{v}_{\text{adapt}}$ (which depends only on $\int_{I_n} \mathbb{1}_{\Omega_{g_i}}\,\mathrm{d}t$).

DOI: 10.1002/fld

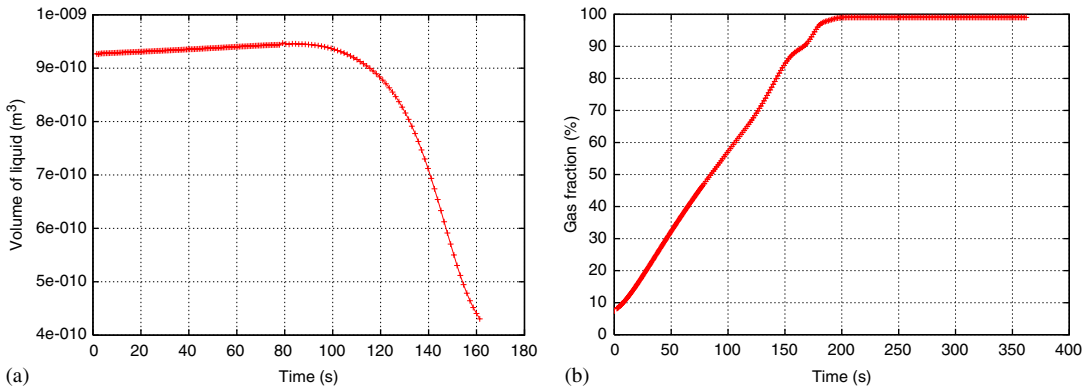

Figure 6. Volume of the liquid matrix and gas fraction evolution, during the expansion of 125 bubbles, with the technique of computational domain expansion. Note that the time span is not the same for the two figures: (a) volume of liquid and (b) gas fraction.

4. Computation of the mesh expansion velocity by solving Equation (17), integrated over I_n.
5. Computation of $\mathbb{1}_{\Omega_{g_i}}$ on I_{n+1}, $i=1,\ldots,Nbb$, by solving Nbb equations like (12).
6. Update the coordinates of the nodes using $X_{|I_{n+1}} \leftarrow X_{|I_n} + |I_n|\mathbf{v}_{\text{mesh}}$.
7. Increment the time interval $I_n \leftarrow I_{n+1}$ and go to 1.

According to this strategy, only the characteristic functions are not constant on a time interval.

3. EXPANSION OF ONE BUBBLE

In this section, a simple 3D analytical model is first developed to describe the expansion of a single bubble into a Newtonian matrix. This model is a simplified version of the cell model due to Amon and Denson in [5, 11]. Contrary to Amon's approach, the bubble is assumed to expand within an infinite Newtonian matrix and surface tension effects are neglected. Thanks to these simplifications, it is possible to know the bubble radius over time and to compare it with our simulations.

3.1. Analytical model

Spherical coordinates (r, ϕ, θ) are used with the origin O chosen at the bubble center. The kinematics of the liquid is ideally described by a purely radial velocity field that depends, such as the pressure, only on the first component r: $\mathbf{v}=(u(r),0,0)$, $p=p(r)$. The initial bubble radius is denoted by R_0, with a corresponding volume V_0 and a gas pressure p_{g_0}. Incompressibility of the liquid takes the form

$$\frac{\mathrm{d}u}{\mathrm{d}r}+2\frac{u}{r}=0, \quad r \geqslant R \tag{18}$$

DOI: 10.1002/fld

With the condition $u(R)=\mathrm{d}R/\mathrm{d}t=\dot{R}$ on the bubble surface, Equation (18) leads to

$$u(r)=\frac{\dot{R}R^2}{r^2},\quad r\geqslant R \tag{19}$$

Because of the spherical symmetry, the momentum balance is described only by a scalar equation:

$$\frac{\mathrm{d}\sigma_{rr}}{\mathrm{d}r}+\frac{1}{r}(2\sigma_{rr}-\sigma_{\theta\theta}-\sigma_{\phi\phi})=0 \tag{20}$$

which is completed with the appropriate boundary conditions:

$$\begin{aligned}\sigma_{rr}(R)&=-p_{\mathrm{g}}\\ \sigma_{rr}(+\infty)&=-p_{\mathrm{ext}}\end{aligned} \tag{21}$$

The Cauchy stress tensor σ is defined by $\sigma=2\eta_l\varepsilon(\mathbf{v})-pI$. Considering expression (19), the form of the strain tensor is

$$\varepsilon(\mathbf{v})=\frac{\dot{R}R^2}{r^3}\begin{pmatrix}-2&0&0\\0&1&0\\0&0&1\end{pmatrix} \tag{22}$$

Consequently, Equation (20) becomes $\mathrm{d}p/\mathrm{d}r=0$. Furthermore, Equation (22) and the second equation of (21) imply $p(+\infty)=p_{\mathrm{ext}}$. Thus, in the liquid, the pressure is constant:

$$p(r)=p_{\mathrm{ext}},\quad r>R \tag{23}$$

Finally, by considering the first condition of Equation (21) and the stress at $r=R$, the growth velocity $\dot{R}$ can be expressed as

$$\frac{\dot{R}}{R}=\frac{p_{\mathrm{g}}-p_{\mathrm{ext}}}{4\eta_l} \tag{24}$$

This analytical model is very useful to understand the expansion of a bubble, and the above results require some comments. First, note the absence of the shear components in (22). Second, since the pressure is constant in the liquid matrix, the liquid–gas interface is a discontinuity surface for the pressure. However, the normal stress is continuous across this surface. Furthermore, the local growth velocity, expressed by Equation (24), depends only on the local pressure difference, which corresponds also to the global one. When $p_{\mathrm{g}}\to p_{\mathrm{ext}}$, $\dot{R}\to 0$ and the bubble stops to grow. If $p_{\mathrm{ext}}=0$, then $\dot{R}$ can never vanish, and the bubble grows indefinitely.

The expression of $R(t)$, solution of Equation (24), takes into account these different behaviors. More precisely, to solve Equation (24), the gas pressure has to be related to the radius and this relation determines the behavior of the bubble. Two cases are investigated. The first one corresponds to a gas pressure that is constant over time. This purely mathematic case (except if we imagine that the number of moles n is proportional to the volume in the ideal gas law $p_{\mathrm{g}}=nRT/V$) leads to a radius that is an exponential function of the time. The second case corresponds to the ideal gas law $p_{\mathrm{g}}V=p_{\mathrm{g}_0}V_0$. Two subcases are then distinguished, following the value of p_{ext}. If $p_{\mathrm{ext}}=0$, then Equation (24) is a homogeneous ordinary differential equation (i.e. without second member) and $R\underset{t\to+\infty}{\longrightarrow}+\infty$, while $p_{\mathrm{g}}\underset{t\to+\infty}{\longrightarrow}0$, the bubble grows indefinitely. Contrary to this situation,

DOI: 10.1002/fld

if $p_{\text{ext}} \neq 0$, then Equation (24) has a second member, and $R \underset{t \to +\infty}{\longrightarrow} R_{\max}$, while $p_{\text{g}} \underset{t \to +\infty}{\longrightarrow} p_{\text{ext}}$, the bubble reaches a maximal radius. These different situations are summarized below.

3.1.1. Constant gas pressure: $p_{\text{g}}(t) = p_{\text{g}}(t=0) = p_{\text{g}_0}$.

$$R(t) = R_0 \exp\left[\frac{p_{\text{g}_0} - p_{\text{ext}}}{4\eta_0} t\right] \tag{25}$$

3.1.2. Ideal gas law: $p_{\text{g}} V = p_{\text{g}_0} V_0$, *with* $p_{\text{ext}} = 0$. The bubble pressure is then expressed by $p_{\text{g}} = p_{\text{g}_0} R_0^3 / R^3$, and

$$R(t) = R_0 \left(1 + \frac{3 p_{\text{g}_0}}{4\eta_0} t\right)^{1/3} \tag{26}$$

3.1.3. Ideal gas law: $p_{\text{g}} V = p_{\text{g}_0} V_0$, *with* $p_{\text{ext}} \neq 0$.

$$R(t) = R_0 \left(\left(1 - \frac{p_{\text{g}_0}}{p_{\text{ext}}}\right) \exp\left[\frac{-3 p_{\text{ext}}}{4\eta_0} t\right] + \frac{p_{\text{g}_0}}{p_{\text{ext}}}\right)^{1/3} \tag{27}$$

Note that the limit radius is computed with Equation (27) when $p_{\text{ext}} \to 0$ is equal to the radius computed with Equation (26).

3.2. Simulations of the expansion of a single bubble (Figure 7(a))

We first underline that in our simulations the bubbles can have any shape. The evolution over time of these bubbles is therefore known through the gas volume fraction $\mathbb{1}^h_{\Omega_{\text{g}}}$. The volume of gas is then equal to $V_{\text{h}} = \int_{\Omega_h} \mathbb{1}^h_{\Omega_{\text{g}}} \, \text{d}\Omega$. When dealing only with one bubble, this volume is of course the volume of the bubble, and the equivalent radius is defined by $R_h = (3V_h/4)^{1/3}$. Furthermore, no specific implementation has been done for the case involving one bubble. Hence, the simulations presented in this section have been performed by using Cartesian coordinates (x, y, z). Figure 7(b) shows the isovalues of the first component of the velocity, $\mathbf{v}_x$, obtained during the simulation of the expansion of one bubble. The velocity vectors have been superimposed on this figure. The scale is not indicated, since the pressure difference $p_{\text{g}} - p_{\text{ext}}$ acts as a scale factor on the velocity. However, the key point of this figure is that the velocity is characteristic of an expansion: it is radial and it reaches its extremal values at the liquid–gas interface.

The three cases already distinguished in the previous section are first investigated. In order to compare the evolution of the bubble radius R_h and the evolution of the bubble pressure with the predictions of the analytical model, the assumption of infinite domain has to be 'satisfied' in our simulations, at least during the first steps of the expansion. The initial bubble radius is therefore chosen small enough when compared with the dimensions of the computational domain. In practice, our simulations and [13] show that, as long as the bubble radius is lower than one-third of the characteristic length of the computational domain, the boundary of this domain does not affect the behavior of the bubble. In the next simulations, the Newtonian matrix has a constant viscosity $\eta_l = 1000$ (Pa s), while the initial bubble radius is $R_0 = 10^{-4}$ (m) and the computational domain is a cube with an initial edge length of 10^{-3} (mm). The comparison between the simulations and

DOI: 10.1002/fld

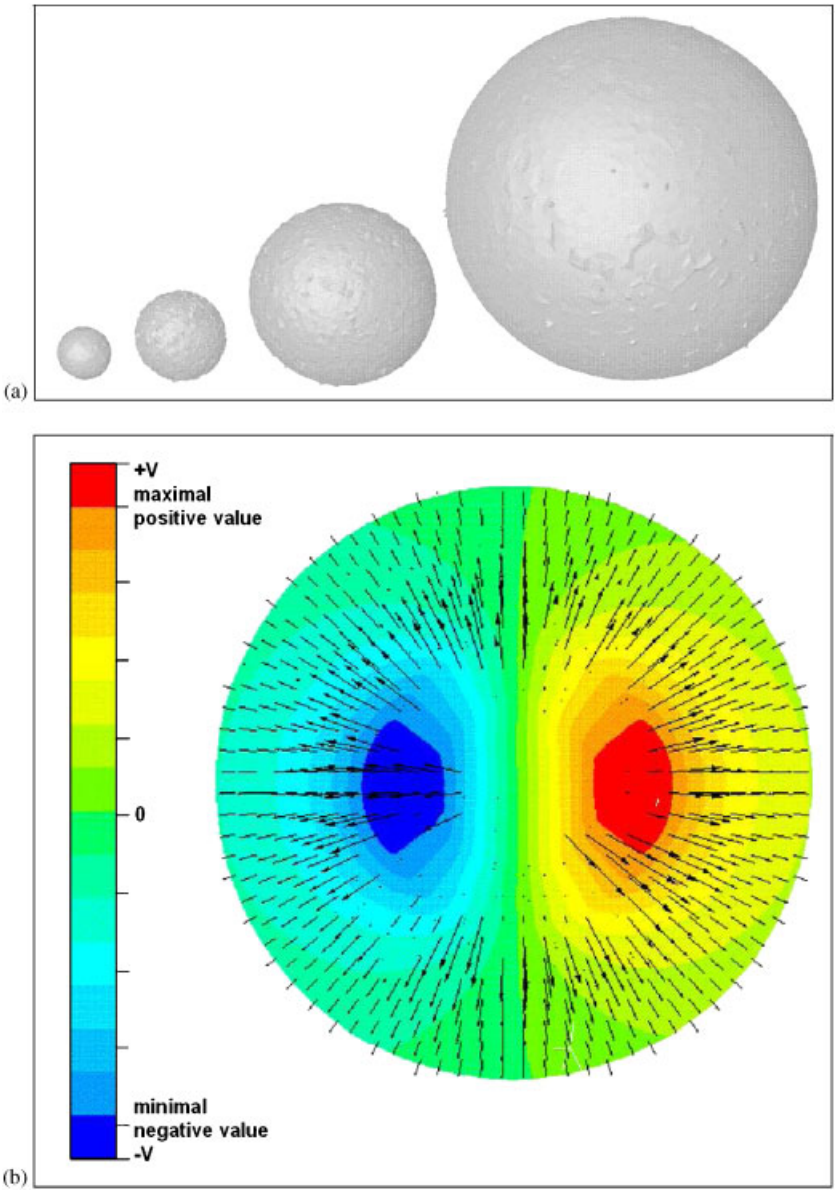

Figure 7. Simulation of the expansion of one bubble: (a) evolution of the level set 0.5 of the bubble characteristic function and (b) computed velocity field (arrows) and its first component (length and time scales are not defined).

the analytical model allows to test the accuracy of our gas–liquid coupling. However, the simulation of the expansion of one bubble is of great interest when dealing with a more complex polymer rheology, as in Section 3.3 or in [10].

DOI: 10.1002/fld

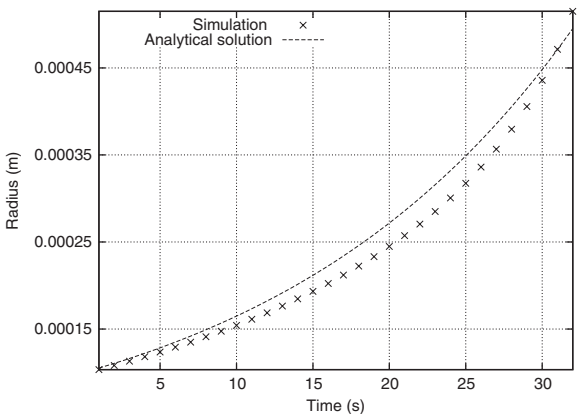

Figure 8. Expansion of one bubble into a Newtonian matrix in the constant gas pressure case: comparison between the computed equivalent radius and the analytical radius provided by Equation (25) with $p_{\text{ext}}=0$.

3.2.1. Constant gas pressure. Let us consider $p_{\text{g}}=p_{\text{g}0}$, with $p_{\text{g}0}-p_{\text{ext}}=200$ (Pa) and $p_{\text{ext}}=0$. This means that the bubble can grow indefinitely. The comparison between the equivalent radius and expression (25) is plotted in Figure 8. A good agreement is shown, as long as the assumption of infinite domain remains valid. As expected, the bubble radius increases exponentially over time.

3.2.2. Ideal gas law with $p_{\text{ext}}=0$. As previously, we have $p_{\text{g}0}-p_{\text{ext}}=200\,\text{Pa}$, with $p_{\text{ext}}=0$. The bubble pressure is now governed by the ideal gas law $p_{\text{g}}V_h=p_{\text{g}0}V_0$, with $V_h=\int_{\Omega_h}\mathbb{1}^h_{\Omega_{\text{g}}}\,\text{d}\Omega$. The comparison between the simulated equivalent radius and the analytical radius given by expression (26) is shown in Figure 9(a), while the comparison between the corresponding pressures is presented in Figure 9(b). The behavior of the simulated bubble corresponds to the prediction of the analytical model: the radius of the bubble increases over time as $t^{1/3}$. The agreement between the theory and the simulation is quite good, as long as the boundary of the computational domain does not affect the bubble expansion (i.e. as long as $t<100\,\text{s}$).

Furthermore, the simulation has been carried out with and without the mesh r-adaptation technique. The advantage of the r-adaption for capturing the cellular structure will be shown in the next section. However, Figure 9(b) shows that the r-adaptation technique does not perturb the simulation of the expansion of one bubble.

3.2.3. Ideal gas law with $p_{\text{ext}}\neq 0$. Let us consider the ideal gas law case with $R_0=0.114$, $p_{\text{g}0}-p_{\text{ext}}=150$ and $p_{\text{ext}}=50$. Contrary to the previous case with $p_{\text{ext}}=0$, the bubble grows until reaching a maximal radius. This radius is found by taking $t\to+\infty$ in expression (27): $R_{\max}=R_0(p_{\text{g}0}/p_{\text{ext}})^{1/3}$.

The comparison between the equivalent radius and the analytical radius, which results from Equation (27), is plotted in Figure 10(a). The corresponding simulated bubble pressure is shown in Figure 10(b). The steady state provided by the simulation corresponds to the state predicted by the analytical model: $R=R_{\max}=0.0181$, while $p_{\text{g}}=p_{\text{ext}}=50$.

DOI: 10.1002/fld

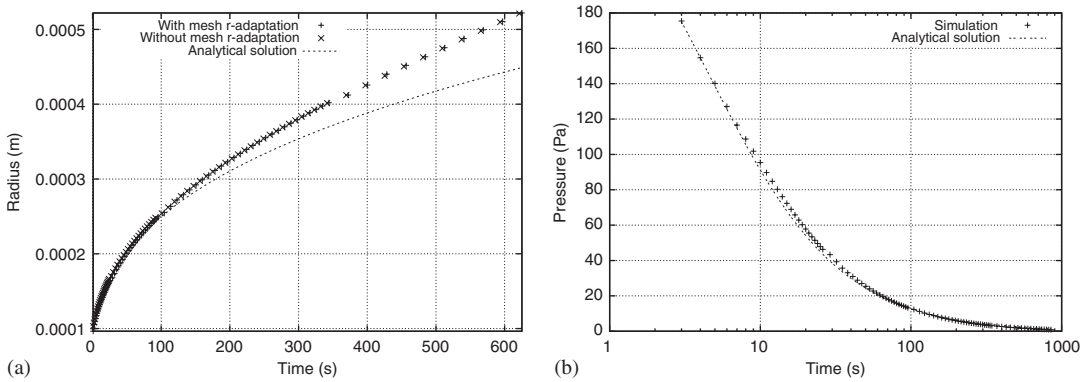

Figure 9. Expansion of one bubble into a Newtonian matrix in the ideal gas law case: comparison between simulation and analytical model with $p_{\text{ext}}=0$ (Equation (26)): (a) radius and (b) pressure.

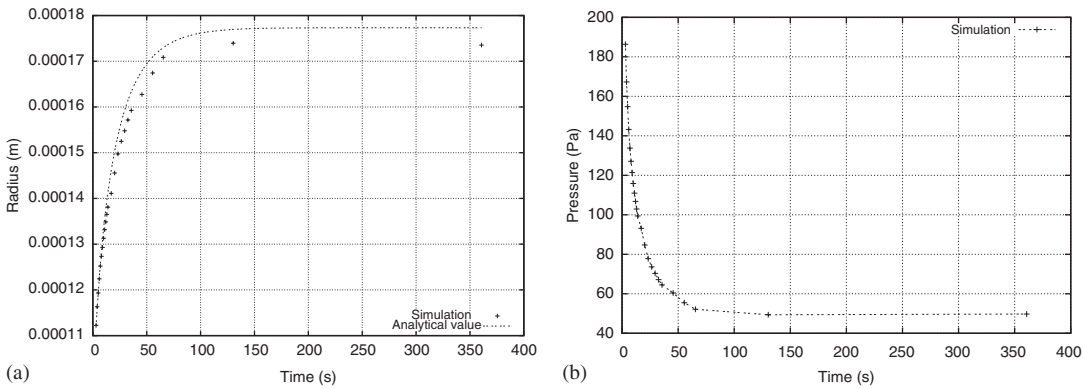

Figure 10. Expansion of one bubble into a Newtonian matrix in the ideal gas law case: comparison between simulation and analytical model with $p_{\text{ext}}=50$ (Equation (27)): (a) radius and (b) pressure.

3.3. Expansion of one bubble into a pseudo-plastic matrix

To conclude the investigation on the expansion of one bubble, we show that the developed numerical methodology can be extended, without any new development, to a case in which the liquid matrix is a pseudo-plastic fluid. The matrix viscosity is then governed by a Carreau's law, which expresses the shear-thinning behavior of a molten polymer by relating the viscosity to the norm of the strain-rate tensor $|\varepsilon(\mathbf{v})|^2=\sum_{i,j}\varepsilon_{ij}^2(\mathbf{v})$:

$$\eta_l(|\varepsilon(\mathbf{v})|)=\eta_0(1+\lambda^2|\varepsilon(\mathbf{v})|^2)^{(m-1)/2} \tag{28}$$

where λ is a characteristic time and m is the shear-thinning exponent, $0\leqslant m\leqslant 1$.

Using Carreau's law in Equations (9) leads to a non-linear system (if $m\neq 1$), which is solved by a Newton–Raphson method. Figure 11 presents the evolution of the radius with the following rheological parameters: $\eta_0=1000$ (Pa s), $\lambda=3.15\times 10^{-3}$ (s) and $m=0.7$. Furthermore, $p_{g0}-p_{\text{ext}}=$

DOI: 10.1002/fld

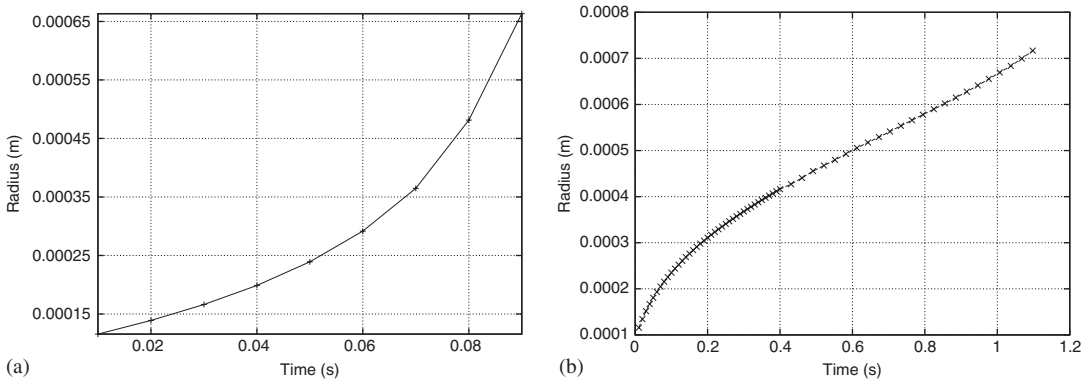

Figure 11. Expansion of one bubble into a pseudo-plastic matrix in the ideal gas law case with $p_{\text{ext}}=0$: (a) constant bubble pressure case and (b) ideal gas law case.

200 (Pa), $p_{\text{ext}}=0$ and $R_0=0.1$ (mm). More precisely, Figure 11(a) illustrates the case with the constant gas pressure, while Figure 11(b) corresponds to the case with the bubble governed by the ideal gas law. Both curves are similar to those obtained in the previous Newtonian cases. Owing to the decrease in the fluid viscosity (shear-thinning behavior), the bubble grows faster in a pseudo-plastic fluid than in a Newtonian fluid.

4. FORMATION OF A TWO-DIMENSIONAL CELLULAR STRUCTURE

Our numerical simulations are first performed in two dimensions. This makes the formation of the foam structure directly visible, without using cutting plane as in three dimensions. Furthermore, a good description of the liquid–gas system can be reached with a reasonable number of elements.

However, our work has been implemented in the numerical software $REM3D$, which is a pure 3D code. For this reason, the computational domain used in the following 2D simulations is a thin parallelepiped $\Omega=[0,1]\times[0,2.10^{-2}]\times[0,1]$, which is meshed with only one element layer (68 000 elements, 23 000 nodes) and is bounded by two symmetry planes (i.e. the boundary condition $\mathbf{v}\cdot\mathbf{n}=0$ is imposed on the planes $\{y=0\}$ and $\{y=2\times10^{-2}\}$).

In spite of the global expansion of the REV, bubbles can escape from it when the motion induced by their expansion cannot be reduced to a homothety. This situation arises when the bubbles are randomly disposed, or when they have no equal volumes (or equal pressures). Since the stress imposed over the boundary of the REV is equal to $-p_{\text{ext}}\mathbf{n}_\Omega$, and since nothing special is done to treat a bubble that is crossing this boundary, such a bubble grows faster than the bubbles situated completely inside the domain (see Figure 12). Consequently, in order to limit the impact of these boundary effects on the final cellular structure prediction, a large number of bubbles have to be considered in the simulations.

The 2D simulation considered in this paper involves 64 bubbles that grow into a Newtonian matrix of viscosity 10^3 (Pa s). The bubbles are initially circular and disposed along a rectangular grid 8×8. Their radii are randomly chosen between 2×10^{-2} and 5×10^{-2} (mm), while the difference between the initial pressure of the gas and the ambient pressure is equal to 200 (Pa):

DOI: 10.1002/fld

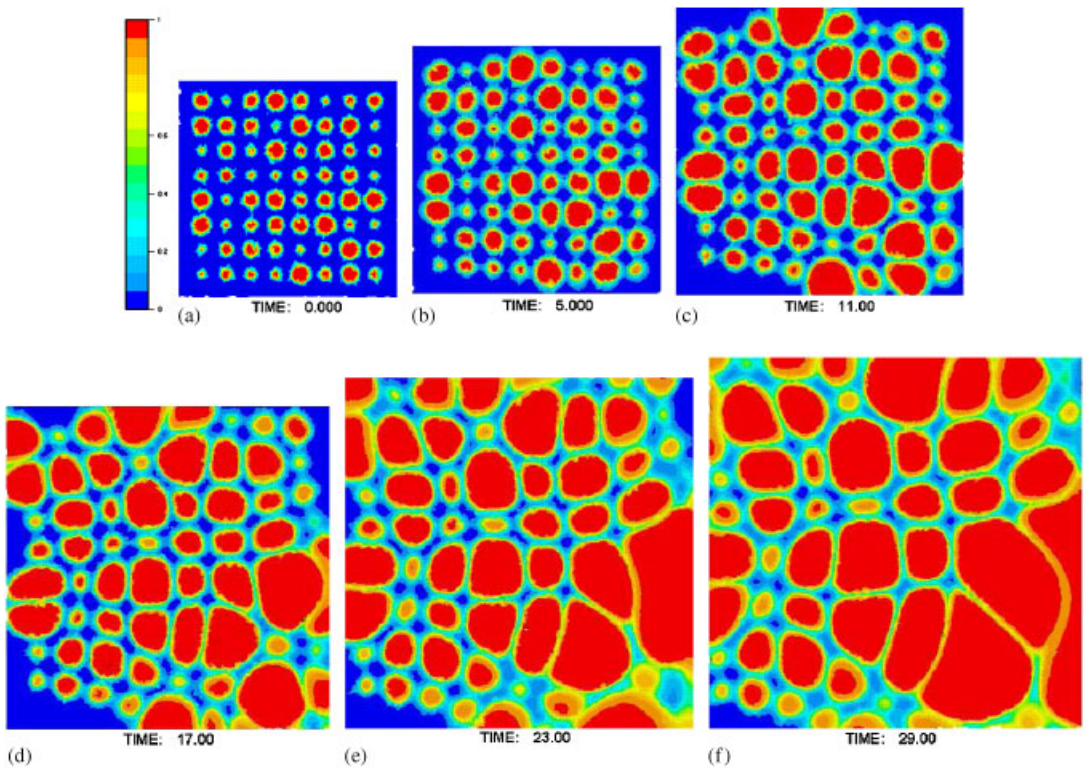

Figure 12. Expansion of a 2D structure composed of 64 bubbles: level sets of the local gas volume fraction. G denotes the global gas fraction. S is the ratio between the actual surface of the computational domain and its initial surface: (a) $G=19\%$, $S=1$; (b) $G=32\%$, $S=1.13$; (c) $G=46\%$, $S=1.3$; (d) $G=60\%$, $S=1.51$; (e) $G=68\%$, $S=1.76$; and (f) $G=76\%$, $S=1.98$.

$p_{g_i}(t=0)-p_{\text{ext}}=200$ (Pa), $\forall i=1,\ldots,64$ with $p_{\text{ext}}=0$ (see analytical model). Figure 12 illustrates the evolution of the gas volume fraction during this simulation. Note that the evolution of the computational domain scale is shown in Figures 12(a)–(f).

The key points of this simulation are summarized below. (a) The bubble expansion is governed by the difference between the inner pressure of the bubble and the normal stress p_{ext} imposed over $\partial\Omega$. The macroscopic parameter p_{ext} (see [5, 11]) depends on the location of the REV in the foam. A more realistic expansion time could be obtained by using a macroscopic model providing the evolution of p_{ext} over time. (b) The velocity field computed during the simulation is presented in Figure 13(a) (at $t=0$). As in the simulations dealing with one bubble, the velocity reaches its local extrema on the bubble surfaces. Furthermore, since $p_{\text{ext}}<p_{g_i}$, the global extrema are reached in the vicinity of $\partial\Omega$ (it is the boundary effect already mentioned). (c) When the simulation starts, the bubbles have the same inner pressure. They grow and interact with each other, and they finally adopt a wide variety of shapes (Figures 12(a)–(f)). The gas pressure corresponding to the final state 12(f) is shown in Figure 13(b). As long as the gas fraction is lower than 65%, the volume of the liquid is well preserved, thanks to the global expansion of the computational domain. The liquid is then trapped mainly between the bubbles. Beyond this value, the peripheral bubbles get

DOI: 10.1002/fld

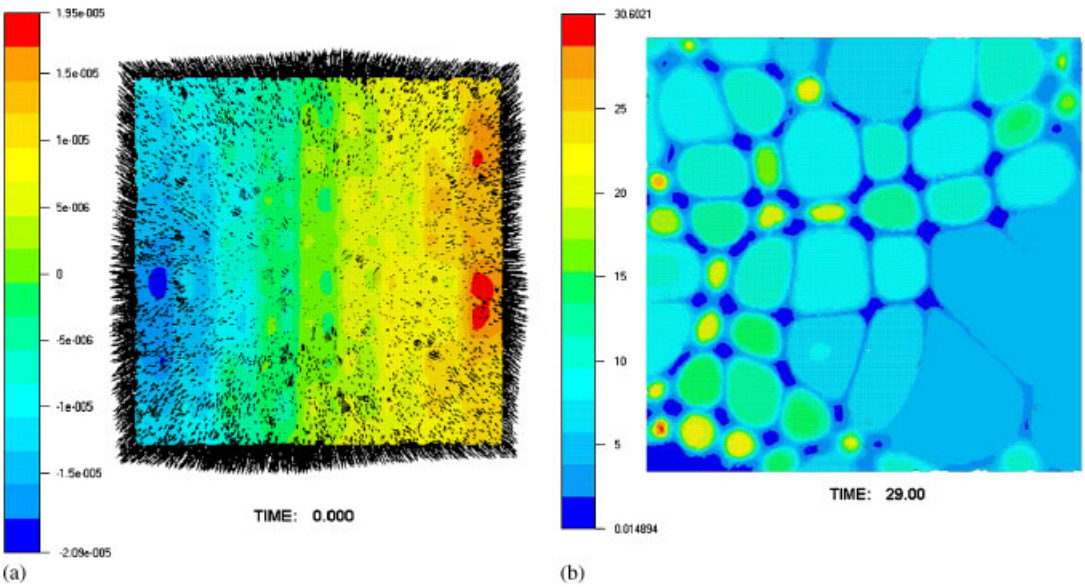

Figure 13. 2D Expansion of 64 bubbles: velocity field (at $t=0$) and gas pressure field (at $t=29$): (a) first component of the velocity field (the units are not defined) and (b) gas pressure field $p_g=\sum_{i=1}^{n} p_{g_i} \mathbb{1}_{\Omega_{g_i}}$.

out of the domain, giving rise to boundary effects: these bubbles grow faster than the others, they coalesce (the value 0.5 of the gas volume fraction disappears), and finally, they perturb strongly the cellular structure. (d) The importance of the mesh motion has to be stressed. First, the necessity of the global mesh expansion appears clearly when we compare the size of Figure 12(a) with the size of Figure 12(f). Thanks to this motion, the computational domain remains representative of the liquid–gas system all along the simulation. Moreover, the mesh corresponding to the final state 12(f) is shown in Figure 14: due to the r-adaptation technique, the interfaces are made directly visible through the stretched elements.

5. FORMATION OF A THREE-DIMENSIONAL CELLULAR STRUCTURE

A 3D simulation requires a larger number of bubbles than a 2D one. The following simulations involve from 100 to 1300 bubbles in a mesh of 550 000 tetrahedrons. In such cases, defining one characteristic function for each bubble, and solving for each of these functions the transport equation (12) on each time interval presents a memory cost and a CPU time dramatically too high. This is why the numerical strategy presented in the first section of this paper is slightly modified to treat a large number of bubbles with a constant memory cost and a constant CPU time.

5.1. Dealing with a large number of bubbles

5.1.1. A rebuilding algorithm. The set of the bubbles is now considered as a single gas phase, which is described through a single characteristic function $\mathbb{1}_{\Omega_g}$ (the local gas volume fraction).

DOI: 10.1002/fld

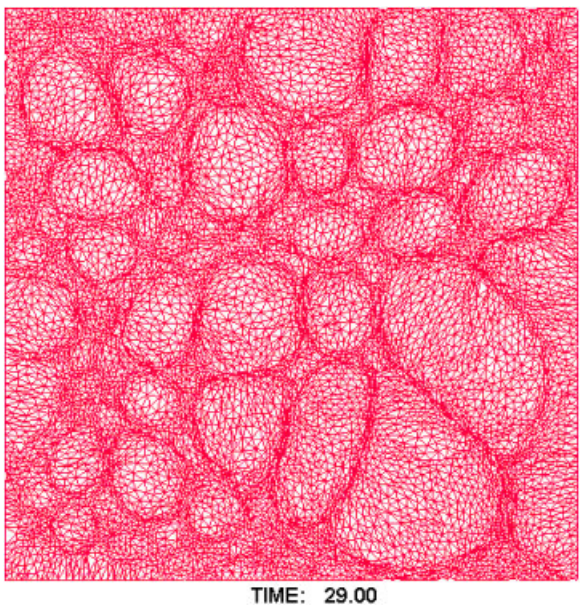

Figure 14. r-Adapted mesh of the computational domain $\Omega = [0, 1] \times [0, 2.10^{-2}] \times [0, 1]$.

$\mathbb{1}^h_{\Omega_g}$ is then advected by solving the transport equation (12) on each interval of time. Based on the values of this function, an algorithm has been developed to rebuild the location of each bubble. This very simple algorithm provides a partition of the mesh $\mathscr{T}_h(\Omega)$ into n subdomains S_i: $\mathscr{T}_h(\Omega) = S_0 \cup \bigcup_{i=1}^{n} S_i$ with $S_i \cap S_j = \emptyset$, $\forall j \neq i$. The subdomain S_0 is the set of the elements which constitute the support of the liquid matrix, while $S_i\,(i > 0)$ is the set of the elements which constitute the support of the ith bubble. The characteristic function of this bubble is then defined as $\mathbb{1}^h_{\Omega_{g_i}} = \mathbb{1}^h_{\Omega_g} \mathbb{1}_{S_i}$. Further details can be found in [13, 20]. It just has to be stressed that this algorithm makes only one loop over the elements. Hence, the CPU time required does not depend on the number of bubbles.

This approach is a geometrical way for solving the problem of describing and advecting several bubbles by using only one function. Compared with the case in which n functions are defined, the rebuilding algorithm implies the following approximation: an element can belong to the support of only one bubble.

5.1.2. Evolution of the gas pressure. Once having rebuilt the n functions $\mathbb{1}^h_{\Omega_{g_i}}$, the pressure of each bubble could be computed by using Equation (3). However, we adopt here a new formulation, which consists in considering a global gas pressure field p_g:

$$p_g(x,t) = \begin{cases} p_{g_i} & \text{if } x \in \Omega_{g_i} \\ 0 & \text{if } x \in \Omega_l \end{cases} \quad \forall x \in \Omega \tag{29}$$

DOI: 10.1002/fld

The mixed weak formulation (9) can easily be reformulated by substituting p_{g} for p_{g_i}. The differential form of the ideal gas law $p_{\mathrm{g}_{|\Omega_{\mathrm{g}_i}}}|\Omega_{\mathrm{g}_i}|=constant$ can be expressed as

$$\begin{gathered}\frac{\partial p_{\mathrm{g}}}{\partial t}+\mathbf{v}_c\cdot\nabla p_{\mathrm{g}}=-p_{\mathrm{g}}E(\nabla\cdot\mathbf{v})\\ p_{\mathrm{g}}(x,0)=\sum_{i=1}^{n}p_{\mathrm{g}_i0}\mathbb{1}_{\Omega_{\mathrm{g}_i0}}(x)\end{gathered}\tag{30}$$

where E is the average operator defined by

$$E(\nabla\cdot\mathbf{v})(x)=\begin{cases}\dfrac{1}{|\Omega_{\mathrm{g}_i}|}\displaystyle\int_{\Omega_{\mathrm{g}_i}}\nabla\cdot\mathbf{v}\,\mathrm{d}\Omega & \text{if } x\in\Omega_{\mathrm{g}_i}\\ 0 & \text{otherwise}\end{cases}\tag{31}$$

Equation (30) is solved by using the space–time discontinuous-Galerkin method. Hence, p_{g}^h is discontinuous in space and time, constant on each element K, and is a polynomial of degree q on an interval of time. The degree q must be equal to the degree used to discretize the gas characteristic function. The discrete form of the average operator is

$$E_h(\nabla\cdot\mathbf{v}_h)_{|K}=\begin{cases}\dfrac{1}{|\Omega_{\mathrm{g}_i}^h|}\displaystyle\int_{S_i}\mathbb{1}_{\Omega_{\mathrm{g}}}^h\nabla\cdot\mathbf{v}_h\,\mathrm{d}\Omega & \text{if } K\in S_i\\ 0 & \text{otherwise}\end{cases}\tag{32}$$

where S_i is the set of elements which constitute the support of $\Omega_{\mathrm{g}_i}^h$.

Further details are given in [20]. It has been shown that the approach, which involves one single function, gives the same results as the classical approach with n functions. Now, the memory cost and the CPU time do not depend on the number of bubbles. Furthermore, considering the gas pressure field makes it possible to have an implicit treatment of the bubble coalescence.

5.2. Expansion of a large and heterogeneous cluster of bubbles

The previous extensions are used to perform the 3D direct simulation of a large number of bubbles which grow within a Newtonian matrix ($\eta_0=10^3$ (Pa s)). When the simulation starts, the computational domain is the unit cube $[0,1]^3$ (mm), meshed with 550 000 tetrahedrons. The bubbles are randomly disposed into this domain. They have the same inner pressure $p_{\mathrm{g}_i0}-p_{\mathrm{ext}}=200$ (Pa), $p_{\mathrm{ext}}=0$ and the same volume.

Figures 15 and 16 illustrate the expansion of 400 bubbles through the evolution of the level set 0.5 of the local gas volume fraction. The global gas fraction G is of 10% when the simulation starts (Figure 15(a)). As in the previous 2D simulation, the bubbles interact with each other and adopt polyhedral shapes (Figure 15(e)). The liquid is then trapped mainly between the bubbles, giving rise to the cellular structure formation. In the first stage of the simulation, the volume of the liquid and the number of bubbles are well preserved, thanks to the global expansion of the REV. The liquid–gas interfaces are then well described, thanks to the r-adaptation technique. Hence, in Figure 15(f), the ratio V between the actual volume of the computational domain and its initial volume (equal to 1) is 1.9. Exactly as in the previous 2D case, beyond a certain gas fraction (about 65% with the used mesh, see Figure 16(a)–(c)) the liquid–gas interfaces are too thin to be

DOI: 10.1002/fld

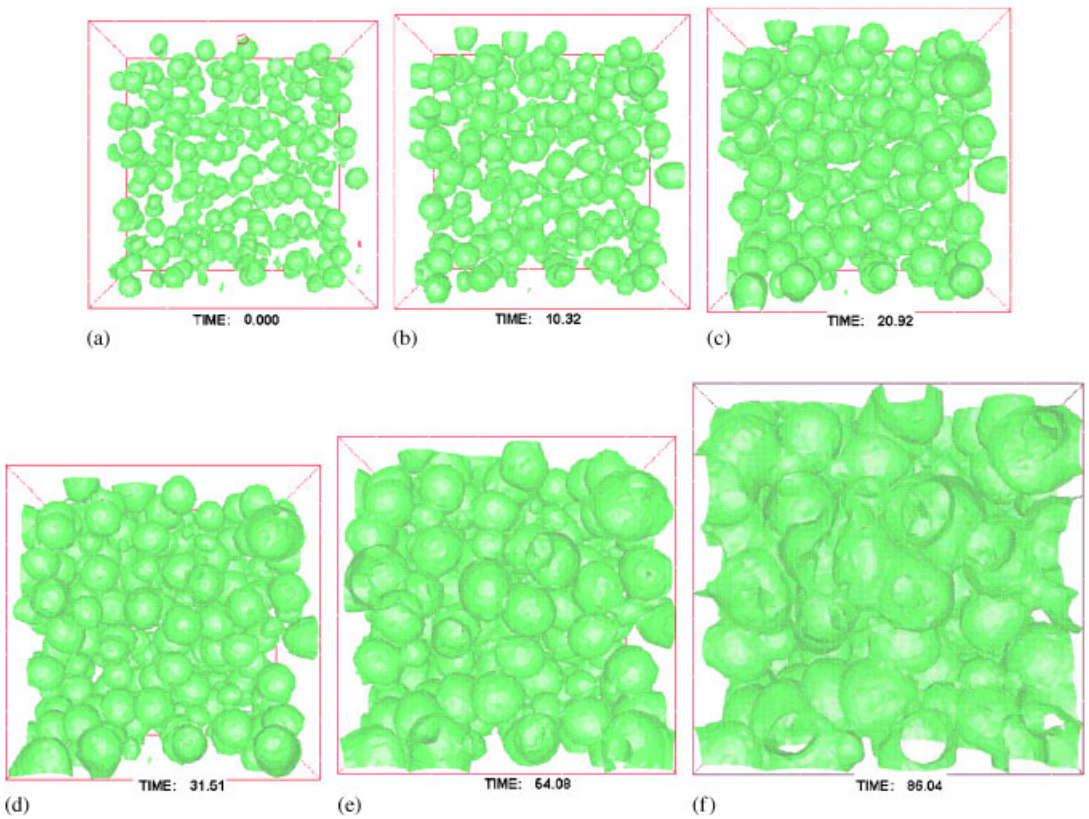

Figure 15. Part I. Expansion of a 3D foam structure composed of 400 bubbles (level set $\frac{1}{2}$ of the local gas volume fraction). G denotes the global gas fraction. V is the ratio between the actual volume of the computational domain and its initial volume. V_f is the volume of the liquid matrix: (a) $G=9\%, V=1, V_f=0.91$; (b) $G=15\%, V=1.06, V_f=0.9$; (c) $G=21\%, V=1.15, V_f=0.91$; (d) $G=28\%, V=1.25, V_f=0.9$; (e) $G=41\%, V=1.76, V_f=1$; and (f) $G=58\%, V=1.89, V_f=0.8$.

correctly described: the level set 0.5 does not permit anymore to represent the interfaces between the bubbles, and shows an apparent bubble coalescence, as already mentioned. At the same time, the boundary effects become important: the peripheral bubbles perturb strongly the formation of the cellular structure.

5.3. Evolution of the global gas fraction

The evolution of the global gas fraction during the simulation of the expansion of 100, 200 and 400 bubbles, respectively, is plotted in Figure 17. In all these simulations, the bubbles have the same initial inner pressure and the same initial volume. Consequently, the initial gas fraction increases when the number of bubbles increases. First, Figure 17 shows that the expansion of the gas is faster when the number of bubbles (and consequently the gas fraction) increases. This is simply due to the fact that the total viscosity of the REV decreases when the fraction of liquid decreases.

DOI: 10.1002/fld

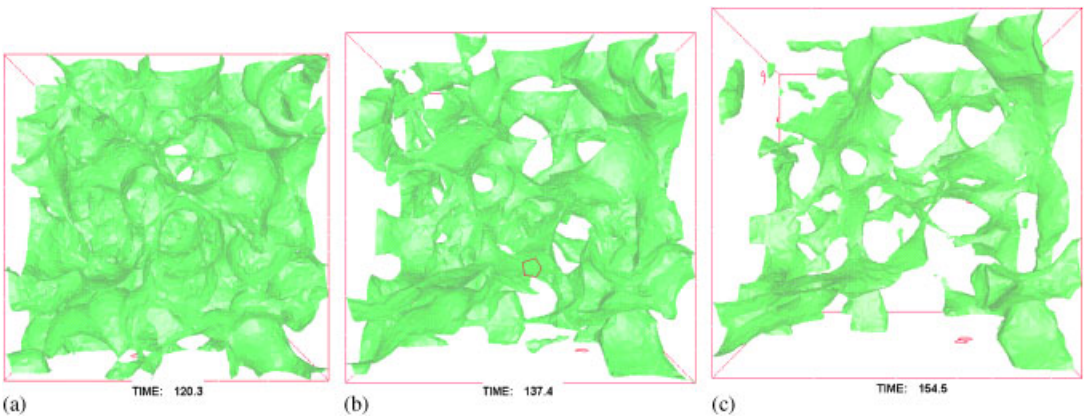

Figure 16. Part II. Expansion of a 3D foam structure composed of 400 bubbles: (a) $G=72\%$, $V=2.52$, $V_f=0.71$; (b) $G=80\%$, $V=3.02$, $V_f=0.6$; and (c) $G=85\%$, $V=3.42$, $V_f=0.51$.

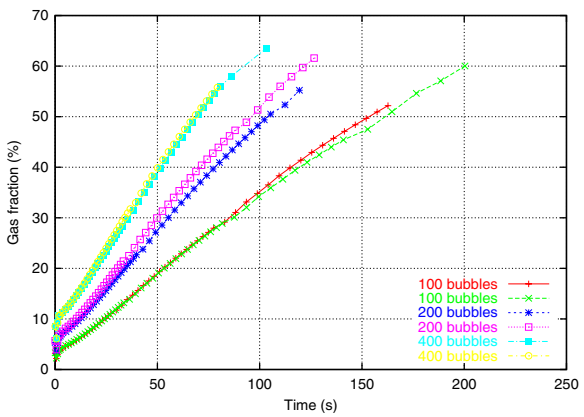

Figure 17. Evolution of the global gas fraction in the REV, during the expansion of 100, 200 and 400 bubbles, respectively.

The second key point of Figure 17 is that, when two simulations deal with the same number of bubbles, they provide an identical behavior of the gas fraction. Hence, in these simulations, the evolution of the gas fraction does not depend on the initial location of the bubbles, but depend only on the number of these bubbles. This point is very important: it proves the reproducibility of the results. In this sense, the computational domain becomes a numerical representative volume with only 100 bubbles.

Finally, we consider simulations performed with from 1 to 1331 bubbles. The evolution of the gas fraction obtained during these simulations is plotted in Figure 18. Contrary to the previous case, the initial fraction of gas is unchanged from simulation to simulation. Consequently, the initial size of the bubbles decreases when the number of bubbles increases. The curve corresponding to the expansion of one bubble is provided by the analytical model (Equation (26)). This curve has

DOI: 10.1002/fld

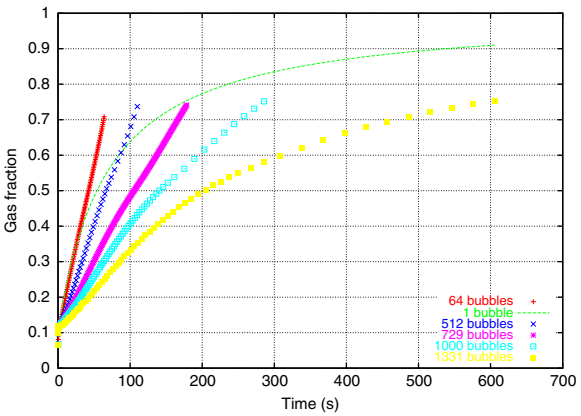

Figure 18. Evolution of the global gas fraction in the REV during the expansion of 1, 64, 512, 729, 1000 and 1331 bubbles. The initial gas fraction is the same for all the simulations.

to be seen as a reference, which allows one to compare the other curves: it represents an 'ideal' case, without interaction between bubbles and without boundary effect.

When considering Figure 18, the effects of the interaction between the bubbles appear clearly: the expansion velocity decreases when the number of bubbles increases. Furthermore, the expansion of 64 bubbles is strongly perturbed when the gas fraction exceeds 40%: beyond this value, the peripheral bubbles (56 if the bubbles are disposed along a rectangular grid $4\times4\times4$) cross the boundary of the computational volume. When the number of bubbles increases, the influence of the peripheral bubbles decreases: as expected, the more the bubbles, the less their expansion is perturbed by the boundary effects (see the curves corresponding to 1000 and 1331 bubbles).

6. CONCLUSION

A finite element strategy has been proposed to directly simulate the 3D expansion of a large and heterogeneous set of bubbles into a polymeric matrix. The relevancy of this approach has been proved through a wide variety of 2D and 3D examples, which ranges from the expansion of one bubble to the expansion of 1300 bubbles. Starting with a computational domain that contains a few percents of gas, the simulations show the formation of a cellular structure. This structure results from the expansion and the interaction of the bubbles. As long as the gas fraction is lower than 65%, the developed numerical tools (space–time discontinuous-Galerkin method combined with an r-adaptation strategy and with a REV expansion motion) make it possible to describe accurately the cellular structure. When the gas fraction exceeds 65%, a thinner mesh is required to avoid the apparent coalescence of the bubbles. In the 3D simulations, the value of 65% is obtained with 400 bubbles and a mesh of 550 000 tetrahedrons. The CPU time of such computations does not depend on the number of bubbles, and is approximately of 12 h with a Pentium 4, 3.4 GHz.

This work has already been used to simulate the cellular structure formation when dealing with chemical reactions [22], with anisothermal expansions [23] or with surface tension effects [13]. However, many ways can be investigated to improve the description of the cellular structure when dealing with a large number of bubbles and with more than 60% of gas. The importance of

DOI: 10.1002/fld

the global expansion of the REV has already been clearly exposed. However, despite this global expansion, the peripheral bubbles still get out of the computational domain, and, as nothing special is done to treat this situation, these bubbles strongly perturb the simulation. A solution to avoid this situation is to embed the REV into a fluid, whose rheology is equivalent to the REV rheology.

Two other numerical ways can be studied to improve our simulations. The first one is to use a level-set method instead of a VOF method for describing the interfaces. The level-set methods do not involve numerical diffusion, and when combined with a mesh adaptation technique, they provide a very good description of the liquid–gas interfaces, as shown in [13] for small bubble clusters. However, even with a level-set method and a mesh adaptation technique, a very thin mesh is still required to describe a large number of bubbles. This is why the second way for improving this work is to use the parallel computing. Indeed, the parallel computing improves the forming process simulations, largely as shown in [24], and allows one to deal with meshes of several million of nodes.

ACKNOWLEDGEMENTS

This work was supported by the EU BIOFOAM Programme, Quality of Life and Management of Living Resources (QLRT-1999-01298).

REFERENCES

1. Han JH, Han CD. Bubble nucleation in polymeric liquids. I. Bubble nucleation in concentrated polymer solutions. *Journal of Polymer Science*: *Part B*: *Polymer Physics* 1990; **28**:711–741.
2. Han JH, Han CD. Bubble nucleation in polymeric liquids. II. Theoretical considerations. *Journal of Polymer Science*: *Part B*: *Polymer Physics* 1990; **28**:743–761.
3. Kraynik AM. Foam flows. *Annual Review of Fluid Mechanics* 1988; **20**:325–357.
4. Shutov FA. Foamed polymers. Cellular structure and proprieties. *Advances in Polymer Science*. Springer: Berlin, 1983; **51**:155–218.
5. Amon M, Denson CD. A study of the dynamics of foam growth: analysis of the growth of closely spaced spherical bubbles. *Polymer Engineering and Science* 1984; **24**(13):1026–1034.
6. Arefmanesh A, Advani SG, Michaelides EE. A numerical study of bubble growth during low pressure structural foam molding process. *Polymer Engineering and Science* 1990; **30**(20):1330–1337.
7. Ramesh NS, Rasmussen DH, Campbell GA. Numerical and experimental studies of bubble growth during the microcellular foaming process. *Polymer Engineering and Science* 1991; **31**(23):1657–1664.
8. Shafi MA, Lee JG, Flumerfelt RW. Prediction of cellular structure in free expansion polymer foam processing. *Polymer Engineering and Science* 1996; **36**(14):1950–1960.
9. Shafi MA, Joshi K, Flumerfelt RW. Bubble size distributions in freely expanded polymer foams. *Chemical Engineering Science* 1997; **52**(4):635–644.
10. Joshi K, Lee JG, Shafi MA, Flumerfelt RW. Prediction of cellular structure in free expansion of viscoelastic media. *Journal of Applied Polymer Science* 1998; **67**:1353–1368.
11. Amon M, Denson CD. A study of the dynamics of foam growth: simplified analysis and experimental results for bulk density in structural foam molding. *Polymer Engineering and Science* 1986; **26**(3):255–267.
12. Han CD. *Multiphase Flow in Polymer Processing*. Academic Press: New York, 1981; 257–340.
13. Bruchon J, Fortin A, Bousmina M, Benmoussa K. Direct 2D simulation of small gas bubble clusters: from the expansion step to the equilibrium state. *International Journal for Numerical Methods in Fluids* 2007; **54**(1):73–101.
14. Everitt SL, Harlen OG, Wilson HJ, Read DJ. Bubble dynamics in viscoelastic fluids with application to reacting and non-reacting polymer foams. *Journal of Non-Newtonian Fluid Mechanics* 2003; **114**:83–107.
15. Arnold DN, Brezzi F, Fortin M. A stable finite element for the Stokes equations. *Calcolo* 1984; **21**(4):337–344.
16. Fortin M, Brezzi F. *Mixed and Hybrid Finite Element Method*. Springer: Berlin, 1991.

DOI: 10.1002/fld

17. Brooks AN, Hughes TJR. Streamline upwind/Petrov–Galerkin formulations for convection dominated flows with particular emphasis on the incompressible Navier–Stokes equations. *Computer Methods in Applied Mechanics and Engineering* 1982; **32**:199–259.
18. Batkam S, Bruchon J, Coupez T. A space–time discontinuous Galerkin method for convection and diffusion in injection molding. *International Journal of Forming Processes* 2004; **7**:11–33.
19. Pichelin E, Coupez T. Finite element solution of the 3D mold filling problem for viscous incompressible fluid. *Computer Methods in Applied Mechanics and Engineering* 1998; **163**:359–371.
20. Bruchon J. Etude de la formation d'une structure de mousse par simulation directe de l'expansion de bulles dans une matrice liquide polymère. *Ph.D. Thesis*, Ecole Nationale Supérieure des Mines de Paris, 2004.
21. Bigot E, Coupez T. Capture of 3D moving free surfaces and material interfaces by mesh deformation. *European Congress on Computational Methods in Applied Sciences and Engineering* (*ECCOMAS*), Barcelona, 2000.
22. Bikard J, Bruchon J, Coupez T, Vergnes B. Numerical prediction of the foam structure of polymeric materials by direct 3D simulation of their expansion by chemical reaction based on a multidomain method. *Journal of Materials Science* 2005; **40**:5875–5881.
23. Bruchon J, Coupez T. Etude 3D de la formation d'une structure de mousse polymère par simulation de l'expansion anisotherme de bulles de gaz. *Revue Mécanique et Industries* 2003; **4**(4):331–338.
24. Digonnet H, Coupez T. Object-oriented programming for 'fast-and-easy' development of parallel applications in forming processes simulation. In *Second MIT Conference on Computational Fluid and Solid Mechanics*, Bathe KJ (ed.), Massachusset Institute. Elsevier: Amsterdam, 2003; 1922–1924.

DOI: 10.1002/fld